

REGULAR ARTICLE

History

Received October 21, 2025

Revised January 6, 2026

Accepted January 14, 2026

Published January 28, 2026

Identifiers

DOI [10.46298/ops.16754](https://doi.org/10.46298/ops.16754)HAL hal-05322136ArXiv [2510.18384](https://arxiv.org/abs/2510.18384)

Zenodo -

Supplementary Material

Licence



© The Authors

Diagnostics of a multicusp-assisted inductively-coupled radio-frequency plasma source for plasma immersion ion implantation

Joel Moreno¹, Marilyn Jimenez¹, Daniel Okerstrom¹, Michael P. Bradley^{1*}, and Lénaïc Couëdel^{1,2}

¹Department of Physics and Engineering Physics, University of Saskatchewan, Saskatoon, SK S7N 5E2, Canada

²Aix-Marseille Université, CNRS, PIIM, UMR 7345, 13397 Marseille Cedex 20, France

Abstract

In this article, we present a detailed characterisation of a multicusp-assisted inductively coupled rf plasma source for plasma immersion ion implantation (PIII). Using laser-induced fluorescence (LIF) and rf-compensated Langmuir probe diagnostics, we measured ion temperature T_i and drift velocity v_z in argon plasmas near an immersed electrode. The multicusp configuration enhances plasma density at low pressure, enabling stable operation down to 0.8 mTorr. Time-averaged measurements show no detectable perturbation near the pulsed electrode, indicating full plasma recovery between high-voltage pulses. LIF-derived potential profiles match Riemann's presheath theory, and ion velocity distributions reveal acceleration consistent with sheath dynamics. These results support the use of LIF for steady-state characterisation of the bulk and presheath regions in PIII systems.

Keywords— Laser-induced fluorescence, inductively-coupled plasma

* Corresponding authors: michael.bradley@usask.ca
lenaic.couedel@usask.ca, lenaic.couedel@cnrs.fr

Cite as: Moreno *et al.*, Diagnostics of a multicusp-assisted inductively-coupled radio-frequency plasma source for plasma immersion ion implantation, *Open Plasma Science* 2, 1 (2026), doi: 10.46298/ops.16754

Contents

1	Introduction	2
2	Experimental setup	3
2.1	Multicusp-assisted rf plasma source	3
2.2	Langmuir probe	4
2.3	Laser-induced fluorescence system	4
3	Results	7
3.1	Bulk plasma measurements: power and pressure dependence	7
3.2	Influence of proximity to electrode (sheath profile)	9
4	Discussion	13
5	Conclusion	14
Acknowledgments		14
References		20

1 Introduction

Modern materials processing demands both precision and efficiency, which in turn require theoretical and computational models validated by empirical data. Among the various surface treatment technologies available, plasma-based processing has emerged as a leading approach due to its versatility and effectiveness across a wide range of applications. These include uniform thin-film deposition [JBT⁺12, MUOG11], multi-tier nanostructure fabrication [BMB⁺17, VPL⁺05], high-aspect-ratio semiconductor etching [QCL⁺91, YC94], and improvements in surface durability and wear resistance [WHCW08, PK02].

Historically, many techniques, such as conventional beamline ion implantation (CBII) [Man92, HO83], chemical vapour deposition (CVD) [ZZZ13], plasma polymerization [BPAK15], plasma oxidation [KJBR23], or physical vapour deposition (PVD) [GYWC20], have been widely used for surface modification. While these methods are still relevant, they present limitations. CBII, for instance, struggles with the uniform treatment of complex geometries and lacks the low-energy ion control needed for ultrashallow junctions in modern microelectronics [And02, KK17]. Vapour deposition techniques, meanwhile, often can suffer from isotropic etching and limited control over ion energy [LL94, AYF08, KBA⁺07, KLW21].

Plasma immersion ion implantation (PIII) offers a compelling alternative. It enables uniform treatment of irregular surfaces, independent control of ion fluence and impact energy, and a relatively simple system design [CB11]. PIII has been successfully applied to tribological enhancement [UBC05], thin-film growth [CPT⁺20], etching [VCHd06, DK13], and the treatment of high-aspect-ratio silicon structures [JLC96]. A more recent application is the use of PIII to study ion bombardment damage to materials intended for fusion reactor plasma-facing components [YB23]. In PIII, the target is immersed directly in the plasma, and ions are accelerated into the surface by the electric fields that naturally occur in the plasma sheath which surrounds the target. In most applications the target is pulsed with a succession of negative-polarity high-voltage (NPHV) pulses, although in some instances the target can be left floating, or be DC-biased. In the pulsed configuration, the ion fluence is determined by the bulk plasma charge density, while the ion impact energy is governed by the applied voltage [And02]. Indeed, the electric field across the sheath between the bulk plasma and a target

surface accelerates the ions for deposition and implantation in the PIII system. Applying NPHV pulses to the target modifies ion energy and fluence, enabling the greater control over implantation depth and ion flux. However, accurate modelling of this process is essential for optimising efficiency and yield.

The first model for HV sheath dynamics was proposed by Conrad *et al.* [CRD⁺87] and later expanded by Lieberman *et al.* [LL94]. Lieberman's model allows the estimation of ion fluence based on steady-state plasma parameters such as density and electron temperature. However, it assumes a stationary and spatially uniform plasma, and a sheath structure that remains consistent across pulses. These assumptions may not hold under realistic operating conditions.

In practice, the NPHV pulse can strongly perturb the plasma [MKO⁺21], even initiating breakdown in the absence of external sources, as seen in pulsed plasma thrusters and high-power impulse magnetron sputtering [GBLH12, LZF⁺20]. This challenges the assumption of steady-state plasma conditions and introduces variability in sheath properties such as potential drop, density, and spatial extent.

Several extensions to Lieberman's model have been proposed, addressing finite pulse rise times [SL91], sheath expansion across multiple pulses [EH92, Woo93], and collisional effects [WMD93]. Time-dependent sheath behaviour is often explored using Particle-in-Cell and Monte Carlo simulations [Woo93, KHG94, CYL95], which show that process efficiency is highly sensitive to pulse repetition rate [TC00, DMRS01]. The repetition rate must be low enough to allow plasma recovery, yet compatible with thermal constraints imposed by target heating [And00]. A sufficiently dense plasma is less affected by the NPHV pulse, improving process reliability.

One effective route to increasing the background plasma density is the use of multicusp magnetic configurations [LM73, JFGB20]. By arranging alternating-polarity permanent magnets to form line or point cusps, electron confinement in the vessel is substantially enhanced due to the strong suppression of cross-field wall losses (ions also benefitting when the magnetic field is sufficiently large). Such configurations are known to sustain large, uniform, and quiescent plasmas suitable for a wide range of processing and source applications [TY93, KKT⁺23, BESF26]. In the context of PIII, this approach is especially attractive: a denser and more stable plasma is noticeably less perturbed by the NPHV pulse, thereby improving overall process robustness.

This article presents the experimental characterisation of a multicusp-assisted, inductively coupled radio-frequency (rf) plasma source designed for PIII applications. The aim is to provide a stable, low-pressure plasma environment suitable for high-fidelity laser-induced fluorescence (LIF) diagnostics. Section 2 describes the experimental setup and the diagnostic tools. Section 3 presents the results and the discussion.

2 Experimental setup

2.1 Multicusp-assisted rf plasma source

The plasma was generated using an inductively coupled radio-frequency (ICP) source operating at 13.56 MHz, designed by Plasmionique Inc. [BS06] for the University of Saskatchewan Plasma Physics Laboratory. The system comprises a stainless steel vacuum chamber, rf power supply with matching network, a pumping system, and a high-voltage pulsing electrode for plasma immersion ion implantation (PIII) studies [Kho19, MKO⁺21, Mor23, YB23].

The cylindrical chamber measures 29.8 cm in diameter and 46.0 cm in height, and includes eight access ports fitted with ConflatTM flanges for diagnostics such as Langmuir probes and optical viewports. To enhance plasma confinement, two rows of eight permanent ferrite magnets were mounted externally with alternating polarity, creating a multicusp magnetic field ranging from approximately 18 G at the chamber edge to $\lesssim 2$ G at the centre.

A stainless steel electrode was inserted into the plasma for ion implantation experiments. With a surface area of 36.45 cm², it could be grounded, DC-biased, or pulsed using a custom-built Marx-bank modulator. For

in the experiments described, the electrode was directly exposed to the plasma to allow direct ion bombardment. It could be manually translated to adjust its depth within the plasma. The high-voltage pulses were applied at 250 Hz with durations of 40 μ s, corresponding to a 1% duty cycle, using a custom Marx-generator type high-voltage modulator [SB07]. A pulse amplitude of -1000 V was used. A laboratory power supply was used for measurements taken with the electrode biased to -30 V DC.

Argon was used as the working gas, with flow rates between 0.5 and 1.0 sccm regulated by an MKS mass flow controller. The vacuum system consisted of a Pfeiffer HiPace 80 turbomolecular pump and a Leybold Turbvac 50, achieving a base pressure of 1 μ Torr prior to plasma ignition. Operating pressures ranged from 0.7 to 2.0 mTorr, chosen to maintain high-confinement (H-mode) conditions.

Plasma was ignited using a 600 W rf power supply connected to a water-cooled planar coil antenna. Impedance matching was handled by a Match Pro CPM-1000 network, which used a combination of fixed and variable capacitors to maintain a 50 Ω input impedance. Reflected power was kept below 5 W and the forward rf power was varied between 350 and 525 W to maximise fluorescence signal intensity.

2.2 Langmuir probe

Plasma parameters, such as the electron and ion densities (n_e , n_i), electron temperature (T_e), and plasma potential (V_{pl}), were measured using a rf-compensated cylindrical Langmuir probe (LP). The probe design follows the rf-compensated model developed by Takashi *et al.* for rf-driven plasmas [TCBH07]. The LP uses a tungsten tip, 0.15 mm in diameter and 6.37 mm in length, chosen to ensure sufficient current collection even in low-density regions of the plasma.

To minimise rf interference, the probe is equipped with four inductors tuned to the first two harmonics of the rf coil (13.56 MHz and 27.12 MHz), acting as band-stop filters. These reduce rf-induced fluctuations of the plasma potential, which can otherwise lead to overestimated electron temperatures [Che03]. Additionally, a copper reference electrode is coupled to the probe tip via an 18 nF capacitor to further suppress rf noise and improve measurement accuracy [CRWAA91].

The probe tip was placed along the central axis of the chamber about 15 cm below the rf antenna (see Fig. 1). Plasma parameters were extracted from the probe IV curves using standard Langmuir analysis [Mer07, Kho19], which assumes a Maxwellian electron energy distribution. This method was found to be accurate for ICPs in this pressure regime [SERO04], and compared favourably with other techniques such as OML [All92], ABR [ABR57], and Druyvesteyn [GPA93], while being computationally efficient for processing large datasets. More details about the probe construction and characteristics can be found in Ref. [Mor23].

2.3 Laser-induced fluorescence system

Figure 2 shows the apparatus used for laser-induced fluorescence (LIF) measurements. This system consists of a tunable diode laser, calibration tools, and signal collection optics. The LIF system is designed to: i) calibrate the laser's relative frequency axis, and ii) detect and amplify the fluorescence signal.

The light source used is a Toptica DL Pro diode laser, tunable in the range of 659–676 nm, with a linewidth of 600 kHz. The laser wavelength is controlled via adjustments to the grating angle, piezoelectric voltage, diode temperature, and current. A mode-hop-free scan over 20 GHz ensures stable and continuous operation. Laser absorption occurs when the wavelength matches the transition energy of a specific excited ion state in its rest frame. The resulting emission intensity from the newly excited state is recorded as a function of the laser wavelength. Accurate wavelength-resolved intensity measurements enable measurement of the Ion Velocity Distribution Function (IVDF) via the Doppler-shift. The second moment of the IVDF provides a measure of the ion temperature T_i , while the peak position of the absorption profile yields the fluid velocity v_i . In our experiments, the laser was tuned to 668.6138 nm, corresponding to the $3d^4F_{7/2} \rightarrow 4p^4D_{5/2}$ transition

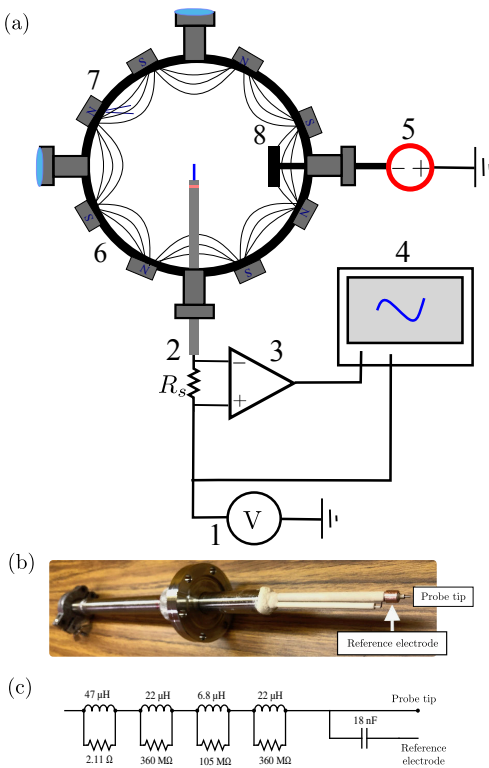


Figure 1: (a) Schematic of the experimental setup for Langmuir probe measurements: 1– Langmuir probe controller adjustable DC power supply; 2– Langmuir probe; 3– Operational amplifier; 4– Oscilloscope; 5– High voltage pulser; 6– Vacuum vessel; 7– Multicusp belt of permanent magnets; 8– Stainless-steel electrode (substrate holder). (b) Picture of the Langmuir probe. (c) Schematic of the probe’s internal circuitry, with four inductors connected in series to reduce the effect of the rf fluctuations on the measured signal.

of Ar^+ (see Fig. 3) [KSB04] and the laser beam was directed perpendicularly to the surface of the stainless-steel electrode.

Calibration is performed using a wavemeter (Bristol 671B, 0.5 pm accuracy) and an iodine reference cell (I-cell). The I-cell is heated to ~ 80 °C to increase the iodine vapour density, enhancing absorption. Four iodine lines near 668.6138 nm (Fig. 2(b) and (c)) assist in wavelength calibration [SR05].

Relative frequency calibration is achieved using a home-made Fabry-Perot etalon, which acts as an air-spaced optical cavity. The etalon consists of two confocal mirrors with $\sim 99\%$ reflectivity at 680 nm and a radius of curvature of 44 mm. The mirrors are mounted on translation stages and separated by 4.2 ± 0.1 cm, giving a free spectral range $\Delta\nu_{FSR} = \frac{c}{4\eta d} \sim 1.78$ GHz, where c is the speed of light in vacuum, d is the mirror separation and $\eta \simeq 1$ is the refractive index of air. The output intensity pattern is detected using a silicon photodiode (Thorlabs FD11A), housed in a metal case with a dedicated battery supply to minimise electrical noise (see Fig. 2(c)). The etalon is enclosed in thermal and electrical shielding to ensure stability. The same photodiode setup is used for the iodine cell. Irregularities in the etalon signal indicate mode-hops, prompting further laser tuning.

Detecting fluorescence from optically-pumped plasma ions requires precise filtering and amplification due to the strong background plasma light and electrical noise from the rf generator. The signal is proportional to the density of argon ions in the metastable $3d\ ^4F_{7/2}$ state, which is populated via electron-impact excitation. The use of multicusp magnetic confinement using belts of alternating-pole permanent magnets allows us to reach relatively high ion density without at low pressure (which minimises quenching) (see Sec. 2.1). Previous studies showed that Zeeman splitting due to a magnetic field of 1 kG caused a broadening of 3.5 pm on the LIF signal [BS03]. Assuming the splitting scales with the applied external magnetic field, this would result in

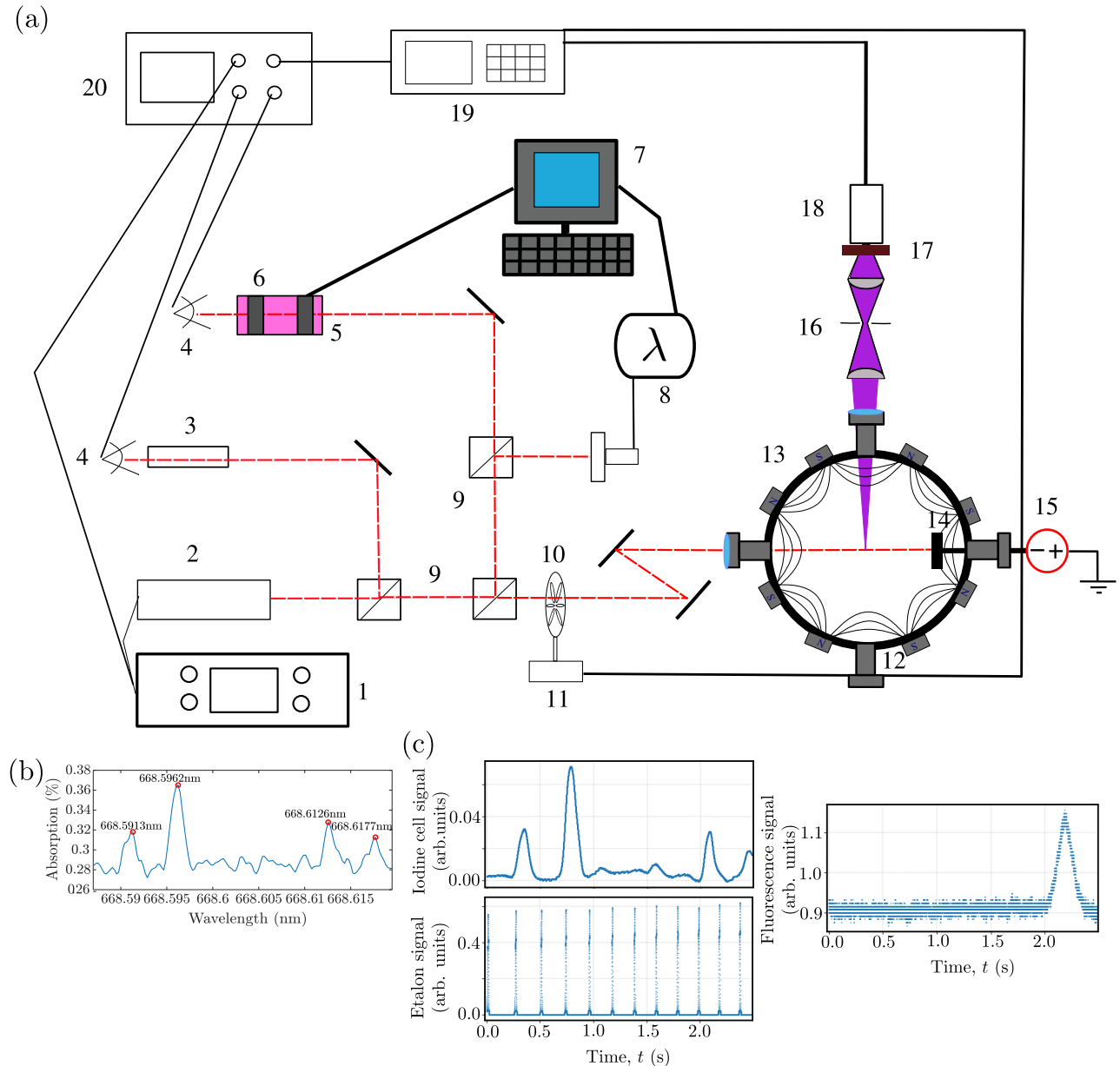


Figure 2: (a) Schematic of the experimental setup for LIF measurements. 1– Laser controller; 2– Laser head; 3– Fabry-Perot etalon; 4– Photodiode; 5– Iodine cell; 6– Iodine cell heater; 7– Computer; 8– Fibre optic head and wavemeter; 9– Beamsplitter; 10– Chopper blade; 11– Chopper controller; 12– Plasma chamber; 13– Multicusp belt of permanent magnets; 14– Pulsing HV electrode; 15– Electrode NPHV pulsing system; 16– LIF collection optics; 17– Narrow bandpass optical filter; 18– Photomultiplier tube; 19– Lock-in amplifier; 20– Oscilloscope. (b) Theoretical iodine absorption spectrum around the 668.6138 nm argon ion transition [SR05]. (c) Raw signal from the LIF setup. From top to bottom: Iodine cell absorption spectrum, Fabry-Perot etalon signal, LIF signal.

a broadening of 0.007 pm in our set-up, which is a negligible affect [TUD07].

The laser beam is modulated by an optical chopper (3.7 kHz) before entering the chamber through anti-reflective coated windows. To minimise reflection from the electrode, the beam is angled slightly off-normal. Fluorescent light is collected using plano-convex lenses and passed through an iris and a narrow bandpass filter centred on the wavelength of the emitted fluorescence photon (442 nm, FWHM 1.0 nm, 45% transmission). The filtered light is detected by a Hamamatsu R3896 photomultiplier tube (PMT), which outputs to a lock-in

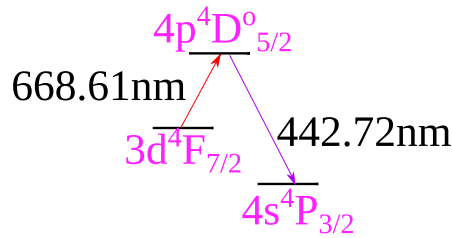


Figure 3: Partial Grotrian diagram for Ar-II transitions.

amplifier (LIA) phase-locked to the chopper frequency. The LIA reduces noise and enhances signal sensitivity. All signals—including from the etalon, iodine cell, laser controller, and LIA—are recorded and averaged by a four-channel oscilloscope to produce the final raw signal [see Fig. 2(c)].

LIF measurements were performed for pressure between 0.7 mTorr and 2 mTorr since pressures above 3 mTorr led to collisional quenching and the disappearance of the LIF signal, while pressures below 0.7 mTorr caused plasma instability and arcing during HV pulsing rendering the measurements unreliable.

3 Results

3.1 Bulk plasma measurements: power and pressure dependence

Langmuir probe measurements conducted at a constant forward rf power of 500 W but varying pressure indicate that the plasma ion density is significantly enhanced in the presence of magnetic cusps. At 0.8 mTorr, the plasma density is almost doubled—from $\sim 6 \times 10^{10} \text{ cm}^{-3}$ to $\sim 1.2 \times 10^{11} \text{ cm}^{-3}$ (see Fig. 4)—demonstrating the improved confinement of the plasma resulting from the introduction of magnetic cusps. This result was expected from the literature [LM73, JFGB20, YTY93, KKT⁺23, BESF26]. It enabled stable plasma operation of our device at low pressures, down to 0.8 mTorr. However, the enhanced confinement due to magnetic cusps diminishes at higher pressures as a result of increased collisionality [JFGB20].

Then, the Langmuir probe measurements focused on characterising the bulk plasma (i.e., at the center of the vacuum chamber) under varying forward rf power (350–525 W) and neutral argon pressure (0.8–2.0 mTorr). These conditions were chosen to allow complementary LIF studies presented later in the section (in this pressure range, we avoid collisional quenching at high pressures (the LIF signal became very weak above 2.0 mTorr) and unstable H-mode of the ICP discharge at low pressures (below 0.8 mTorr)). Rf-compensated Langmuir probe measurements gave us n_i , n_e , T_e , and V_{pl} (Figure 5) while LIF measurements focused on T_i and the ion drift velocity v_z .

Langmuir probe measurements must be interpreted carefully. While electron saturation current $I_{e,sat}$ can indicate n_e , this is reliable only at low densities and pressures, where the electron mean free path is long [Che03]. At higher densities, the probe can drain the plasma, altering its equilibrium. Additionally, due to experimental noise and probe contamination, the identification of $I_{e,sat}$ can be inaccurate [JYG⁺23]. Therefore, ion current collection is often preferred for estimating density (here we used Orbital Motion Theory to extract plasma density from the ion current [Che03]), especially given plasma quasineutrality [Che03]. Additionally, due to the inherent noise of our data acquisition system, the error bars on the Langmuir probe results were quite large and the obtained values thus served as order-of-magnitude estimates only. The observed trends are (see Fig. 5):

- V_{pl} decreases with pressure and is almost independent of the forward rf power.
- n_i (and n_e) increase with power and pressure (n_e is approximately five times lower than n_i with much

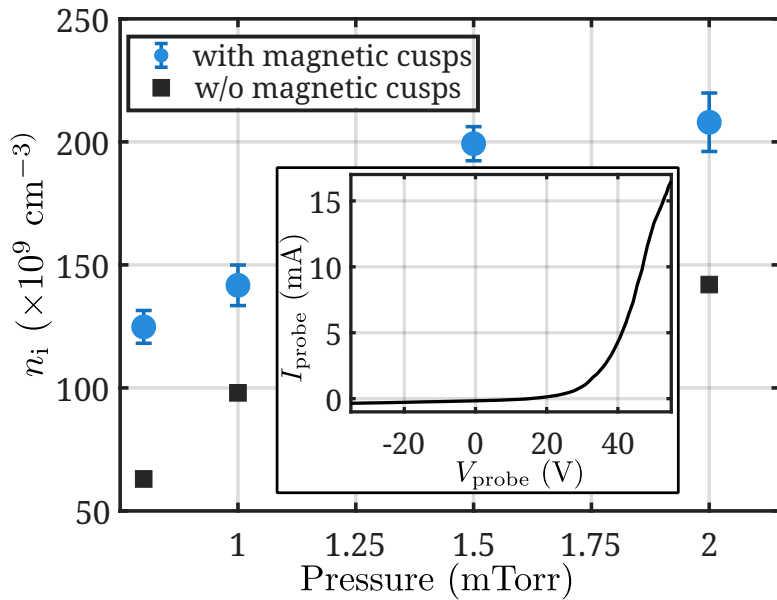


Figure 4: Ion density n_i with (blue circles) and without (black square) magnetic confinement was measured at various pressures at 500 W input power using a Langmuir probe positioned along the discharge axis. For improved visual clarity, error bars for the measurements without magnetic cusps are omitted; however, they are comparable in magnitude to those associated with the measurements taken in the presence of magnetic cusps. The inset shows a Langmuir probe characteristics at a pressure of 0.80 mTorr.

larger errorbars, likely due to noise in the IV characteristics and probe-induced perturbations that drain the plasma and alter its equilibrium state [Che03]).

- Measured electron temperature (T_e) ranged from 5 to 7.5 eV and was found to remain relatively constant.

Our findings are generally consistent with results obtained from Langmuir probe diagnostics reported in the literature [LL94, GPA02]. Prior studies suggest that the electron temperature (T_e) is primarily governed by pressure, increasing as pressure decreases, while exhibiting only a weak dependence on rf power within certain operational regimes [HBU⁺96, HGWC93]. In our measurements, however, this trend is not clearly discernible due to the large error bars. In contrast, electron density (n_e) was found to be strongly influenced by both pressure and power, increasing with higher rf power and higher pressure [HBU⁺96]. Across multiple experiments, T_e typically ranged between 2–7 eV [MI96, HGWC93]. At low rf power, T_e could be smaller for the highest pressure (errorbars are too large to conclude), whereas at high rf power, there are no observable differences between pressure. The interplay between neutral gas heating and stepwise ionisation, which modifies the electron energy distribution, is known to play a role on the pressure/power dependence of the electron temperature [LSK⁺17]. Neutral gas dynamics also play a significant role: neutral density is often depleted in the plasma center due to heating from collisions with charged particles [HBU⁺96]. Furthermore, the plasma heating mechanism transitions from stochastic heating at low pressure to collisional heating at higher pressures. This shift affects how electrons gain energy, particularly in relation to nonlocal electron kinetics and ambipolar potential barriers [KKK⁺21].

The normalised Ion Velocity Distribution Functions (IVDFs) presented in Figure 6(a) exhibit a discernible broadening as the applied power increases, indicative of a higher ion temperature (T_i). This interpretation is corroborated by Figure 6(c), which demonstrates a slight increase in T_i from ~ 0.09 eV to ~ 0.11 eV over the investigated power range. The dependence of T_i on pressure, also shown in Figure 6(c), is unclear and no trend can be directly seen. These findings are broadly consistent with previous investigations, which reported ion temperatures in the range of 0.04–0.08 eV and observed similar trends of increasing T_i with power [Heb96,

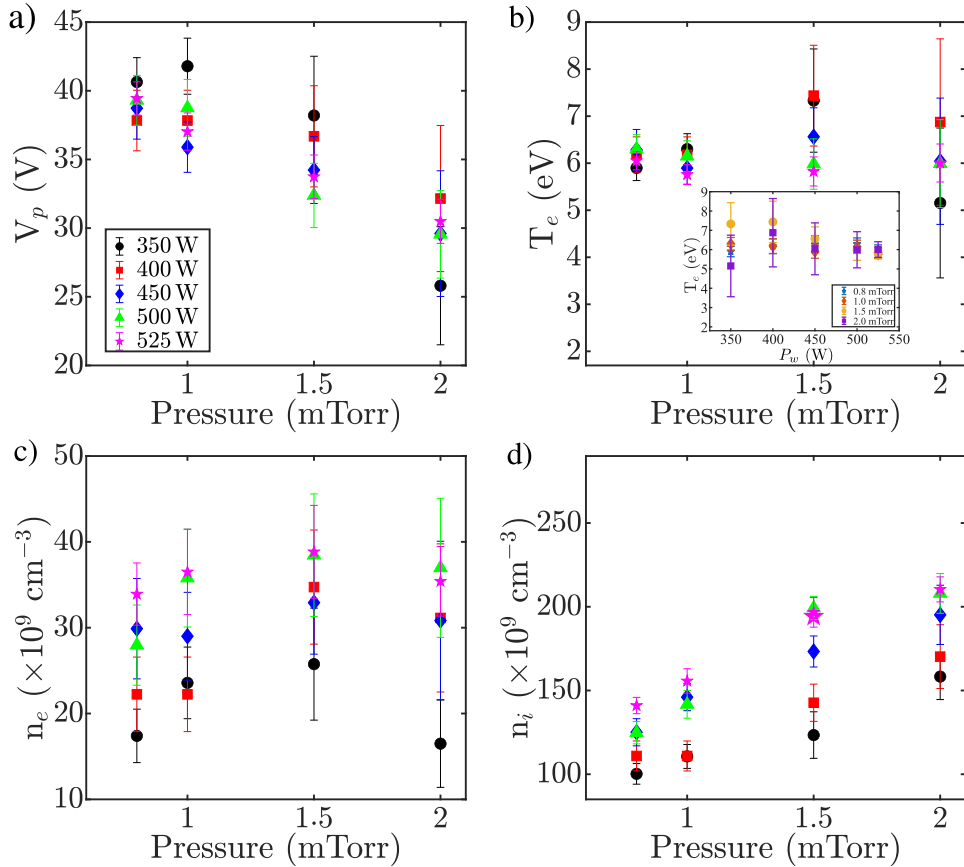


Figure 5: Langmuir probe measurements as a function of rf power and pressure: (a) plasma potential V_{pl} , (b) electron temperature T_e , (c) electron density n_e , and (d) ion density n_i . The electron density n_e is approximately five times lower than the ion density n_i , likely due to probe-induced perturbations that drain the plasma and alter its equilibrium state [Che03]. For clarity, the inset in (b) also shows T_e as a function of the rf power P_w .

SVV⁺97, JCM06]. Jun *et al.* [JCM06] reported that for pressures exceeding approximately 1.5 mTorr, T_i begins to decrease but our current measurements are unable to confirm this finding. Therefore, the behaviour of T_i at higher pressures remains an open question and merits additional study.

The directed (drift) ion velocity remains slightly negative, approximately -75 m/s, across all investigated powers and pressures [Figure 6(b)]. In an idealised symmetric discharge, the drift velocity at the plasma centre would be expected to be exactly zero. The observed deviation is likely attributable to asymmetries introduced by diagnostic access ports and other structural features of the vacuum vessel, as well as a potential lateral displacement of the LIF interrogation volume from the discharge axis.

3.2 Influence of proximity to electrode (sheath profile)

This section characterises the ion dynamics in the vicinity of an immersed electrode in our multicusp-assisted inductively coupled argon plasma, with three aims: (i) determine whether time-averaged LIF can reveal signatures of the high-voltage (HV) implantation sheath under negative-polarity pulses; (ii) map the directed ion velocity v_z and infer the steady-state presheath/sheath potential profile for grounded and DC-biased conditions; and (iii) examine the evolution of the ion temperature T_i as the measurement volume approaches the electrode.

Experiments were performed at $P_{\text{RF}} = 500$ W and $p = 0.8$ mTorr. The electrode was set to: (a) ground,

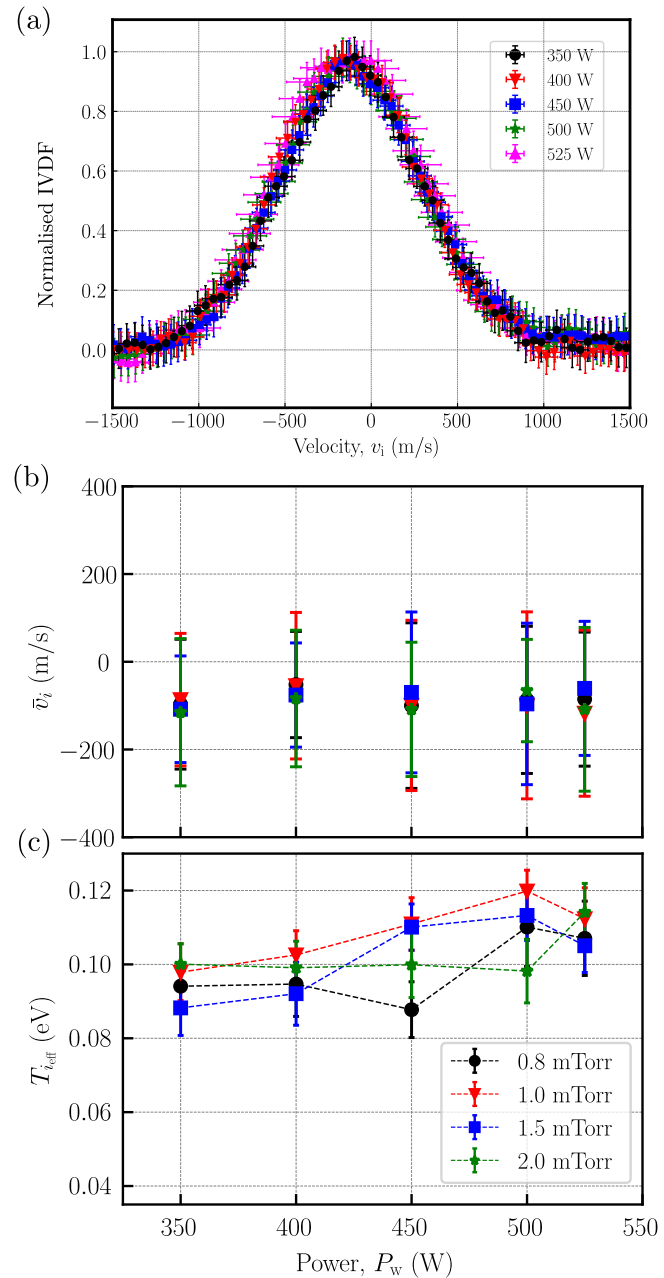


Figure 6: (a) Normalised IVDFs at 0.8 mTorr for various rf powers. (b) Ion drift velocity as a function of power for different argon pressure. (c) Ion temperature as a function of power for different argon pressure.

(b) -30 V DC, and (c) pulsed at -1 kV with 40 μ s duration at 250 Hz (1% duty cycle). Spatial scans were executed from $z = 0.1$ to 2.0 cm in front of the electrode (finer steps of 0.1 cm within 0.1 – 0.5 cm).

The time-averaged fluorescence profiles at 1 mm of the electrode surface for different bias are shown in Fig. 7. No detectable deformation under HV pulsing nor the DC bias can be seen. Consistently, $v_z(z)$ is essentially indistinguishable between grounded, -30 V DC, and pulsed case. Within the averaging limits, this supports the common approximation that bulk parameters between pulses are only weakly perturbed.

Figure 8 presents the normalised experimental IVDFs at different distances z from the grounded electrode. As z decreases, the peak of the distribution shifts towards higher velocities, indicating ion acceleration

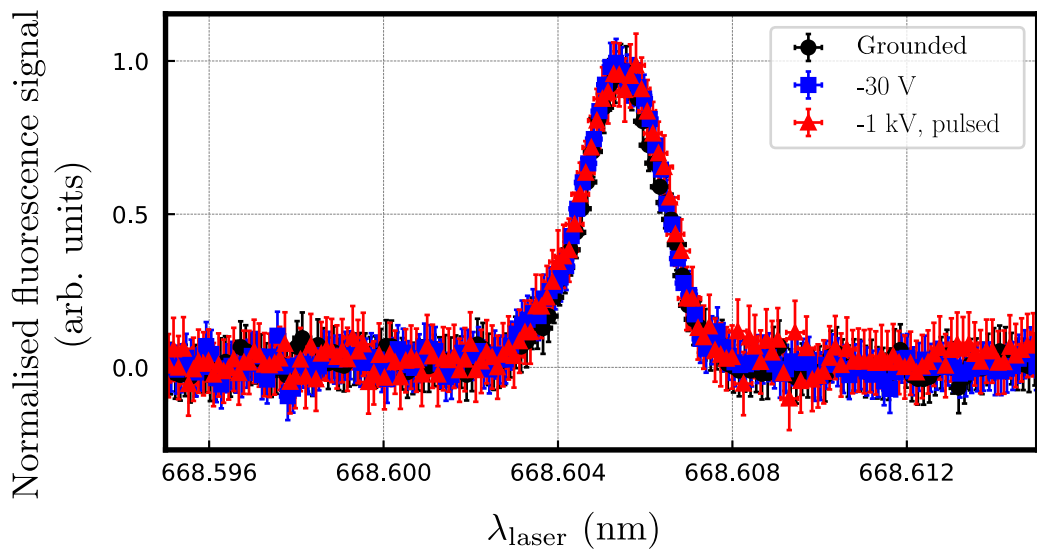


Figure 7: Normalised fluorescence profiles as a function of laser wavelength λ_{laser} measured at a distance of 1 mm from the electrode surface. Three conditions are shown: grounded electrode (black), DC-biased electrode at -30 V (blue), and electrode subject to -1 kV pulsed bias (red). For clarity, the spectral resolution in λ_{laser} has been reduced in the plot.

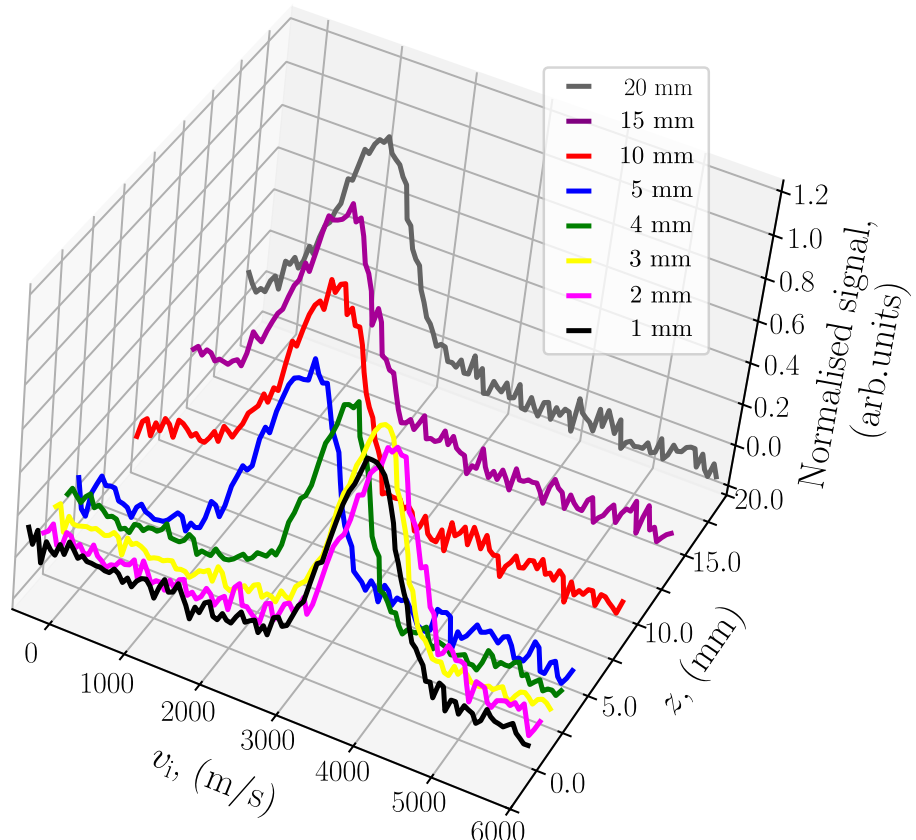


Figure 8: Normalised ion velocity distribution functions (IVDFs) measured at various distances z from a grounded electrode. The profiles illustrate the evolution of the IVDF shape and peak position as the electrode is approached. For clarity, the errorbars ($\sim 5\%$) have been removed.

towards the electrode in the presheath region. The IVDF width appears to decrease progressively down to approximately $z = 4$ mm; beyond this point, the trend becomes less clear. The increase in ion velocity observed close to the target is attributed to ion acceleration by the electric field in the presheath region. The measurements concern metastable argon ions ($\text{Ar}^{+*}, 3d^4F_{7/2}$), which represent less than 1% of the total ion population [SVV⁺97]. Due to their short mean free paths, these ions are generated locally via electron impact, rather than being transported from outside the presheath. The absence of a zero-velocity component in the IVDFs confirms that excitation occurs after acceleration. As a result, the measured velocity distribution of metastable ions should accurately reflect that of ground-state argon ions [SVV⁺97].

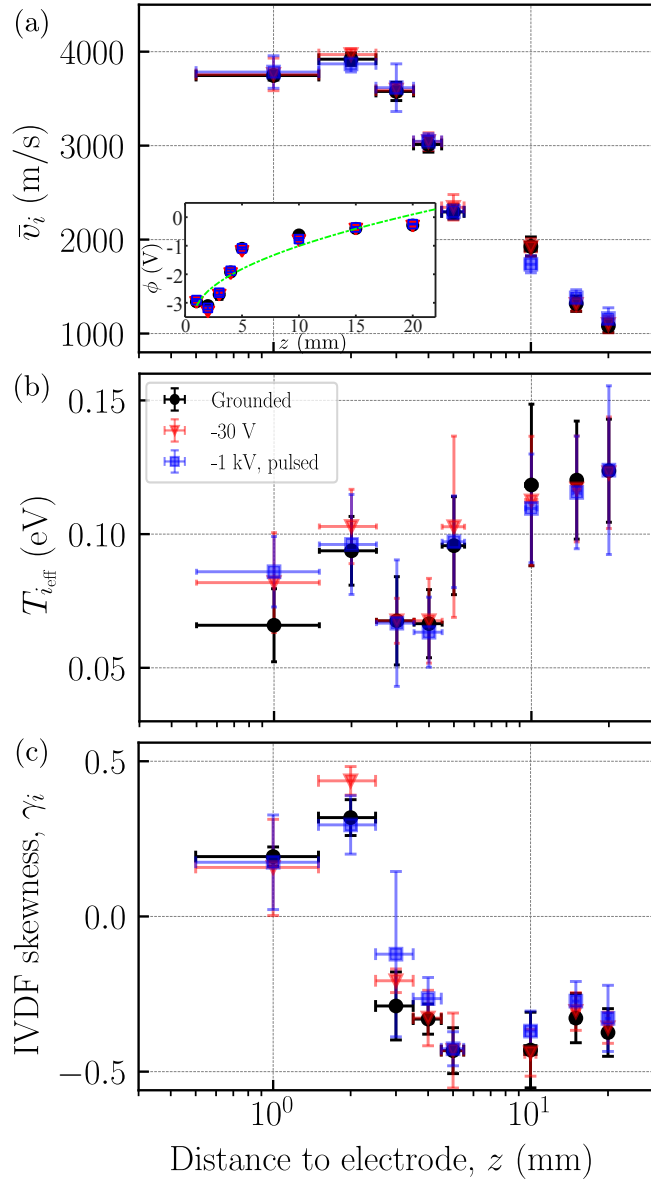


Figure 9: Spatial evolution of IVDF parameters as a function of distance z from the electrode: (a) mean ion velocity \bar{v}_i , (b) effective ion temperature $T_{i,\text{eff}}$, and (c) skewness γ_i . Results are shown for grounded, DC-biased, and pulsed-bias conditions. The inset in (a) shows the electric potential profile assuming collision-less ions and the dashed green line is the fit using Eq.1.

Equivalent measurements were performed for an electrode biased at -30 V and for an electrode subject to -1 kV pulsed bias (red curves). Each IVDF was fitted with a skewed Gaussian function to quantify

asymmetry. From these fits, the mean ion velocity \bar{v}_i , the effective ion temperature $T_{i,\text{eff}}$, and the skewness γ_i were extracted as functions of z (Fig. 9). The profiles for all electrode biases are nearly identical, reinforcing the previously-noted assumption that bulk plasma parameters remain largely unperturbed between short-duty-cycle pulses.

The mean ion speed increases monotonically as z decreases, approaching the theoretical Bohm velocity u_B . Based on Langmuir probe measurements at $p = 0.8$ mTorr and $P_{\text{RF}} = 500$ W (Sec. 3.1), the Debye length is estimated as $\lambda_D \approx 40\text{--}80 \mu\text{m}$, the Bohm velocity as $u_B \approx 3\text{--}4 \text{ km s}^{-1}$, and the steady-state sheath thickness as $S_{\text{is}} \approx 0.3\text{--}0.6 \text{ mm}$ [MP12]. LIF measurements indicate that ions reach u_B at $z \simeq 0.1\text{--}0.2 \text{ cm}$, which is slightly larger than the estimated sheath length but remains consistent within the large theoretical uncertainties and the modified conditions introduced by the presence of the electrode.

The fits of the IVDFs indicate that T_i decreases from $z = 20$ to 4 mm and then increases from $d = 4$ to 2 mm (Fig. 9(b)) and seems to decrease again at $z = 1 \text{ mm}$. This non-monotonic trend contrasts with several earlier reports of monotonically increasing T_i towards a boundary in other devices/conditions [BCD95, SNTG91, OAH01, OH05]. However, the neutral gas temperature profile in the discharge is unknown and it is reported in the literature that the neutral temperature has a maximum in the centre of the discharge and decreases towards the edge [Heb96]. Ion-neutral collision might therefore explain why the ion temperature decreases towards the electrode.

Figure 9(c) presents the evolution of the skewness of the IVDF as a function of the distance z from the electrode. Between $z = 20 \text{ mm}$ and $z = 5 \text{ mm}$, the skewness is negative and decreases from approximately 0.35 to 0.45, indicating a slight deviation from a Maxwellian distribution. A negative skewness implies an asymmetry in the IVDF, with a higher population of slow ions compared to fast ions. This feature may be attributed to low-velocity ion populations generated by ionisation or charge-exchange processes [CBSD06, CM15, YHS15]. As the distance to the electrode decreases further, the skewness increases, reaching zero at $z = 3 \text{ mm}$ (Maxwellian distribution) and becomes slightly positive at shorter distances, where the fast-ion side dominates. It is important to note that the spatial resolution ($\Delta z \sim 0.5 \text{ mm}$) can introduce artificial broadening of the IVDF due to averaging over the detection volume. Near the target, where ion velocity increases rapidly, this effect may distort the measured IVDF towards higher velocities, leading to an overestimation of both the drift velocity and the ion temperature [vdG97].

4 Discussion

At a pressure of 0.8 mTorr , the neutral density is approximately $n_n \approx 3 \times 10^{19} \text{ m}^{-3}$. Assuming an ion-neutral collision cross section of $\sigma \sim 10^{-18} \text{ m}^2$ [LL94], the corresponding ion mean free path is $\lambda_{i,\text{MFP}} \sim 30 \text{ mm}$ [LL94]. This suggests that most LIF measurements are performed well within the spatial extent of the presheath. Using order-of-magnitude inputs from probe diagnostics at 0.8 mTorr and 500 W (Section 2.2), the following plasma parameters are also estimated: Debye length $\lambda_D \approx 50 \mu\text{m}$, ion sound speed $u_B \approx 3.9 \text{ km s}^{-1}$, and ion sheath thickness $S_{\text{is}} \sim 0.3 \text{ mm}$. Using energy conservation, the local potential can be inferred from the axial ion velocity via $\phi_{\text{ps}}(z) = \frac{M_i \bar{v}_i^2}{2e}$. The resulting LIF-derived potential profile can be fitted reasonably well with Riemann's analytical model for a weakly collisional presheath [Rie91, LKL⁺22]:

$$\phi(z) = T_e \sqrt{\frac{(z - z_0)}{\lambda_{i,\text{MFP}}}} + \phi_0, \quad (1)$$

where z_0 is the position of the sheath–presheath boundary. The fit (inset of Fig. 9(a)) yields an effective electron temperature of $T_e \approx 2.8 \text{ eV}$ (within a factor of ~ 2.2 of probe (consistent with typical probe uncertainties) and close global model estimates ($\sim 2.5 \text{ eV}$ using the model described in Ref. [LL94])), an ion neutral mean free path $\lambda_{i,\text{MFP}} \sim 12 \text{ mm}$ (consistent with our previous estimate), and a sheath presheath boundary

at ~ 0.8 mm (in reasonable agreement with our estimate). The measured ion drift velocity $v_z(z)$ reaching the Bohm speed u_B and the closeness of the LIF-derived potential profile $\phi(z)$ with Riemann's model confirm the successful access to the presheath region.

The non-monotonic behaviour of $T_i(z)$ near the electrode likely results from a combination of factors: measurement noise, deviations from Maxwellian IVDFs, metastable-state kinetics, and spatial variations in neutral gas temperature. The observed IVDF skewness suggests the presence of low-velocity ion populations due to ionisation and charge-exchange processes [BCD95, SNTG91, OAH01, OH05].

Comparisons between grounded, DC-biased, and NPHV-pulsed conditions show that steady-state plasma parameters remain largely unaffected by the NPHV pulses, consistent with the short duty cycle used. In the context of PIII, it tends to confirm that the use of multicusp magnetic configurations allowing a denser and more stable plasma is less perturbed by the NPHV pulse and is interesting for the process robustness. Nevertheless, for NPHV pulses of $V_s = -1000$ V, the estimated sheath thickness (~ 2 mm) lies within the LIF collection volume. However, the corresponding Doppler shift (~ 100 GHz) exceeds our laser's tuning range, limiting the direct observation of NPHV sheath dynamics. Time-resolved LIF with extended frequency access is needed to capture transient effects during NPHV pulses.

5 Conclusion

In this study, laser-induced fluorescence was used to investigate ion dynamics in the bulk and in the presheath regions of a multicusp-assisted ICP discharge. The system successfully measured T_i and v_z in both bulk plasma and near an immersed electrode.

The key findings are:

- Ion temperature T_i increases with rf power in the bulk plasma, consistent with prior studies. No dependence of T_i on pressure could be clearly identified.
- Ion drift velocity v_z remains near zero in the bulk but increases near the electrode, reaching u_B at ~ 1 mm from the electrode surface ($\gtrsim 20\lambda_D$).
- Potential profiles derived from LIF match relatively well the Riemann's weakly collisional presheath model.
- No time-averaged distortion was observed under NPHV pulses, confirming plasma recovery between pulses and the suitability of a multicusp-assisted ICP discharge for reliable PIII.

Future work should focus on improving signal-to-noise ratio and improving the diagnostics capabilities to improve the accuracy of the measurements and enable time-resolved LIF and capture the NPHV sheath dynamics. Additional parameter scans and collisional-radiative modelling will help clarify ion temperature behaviour and metastable kinetics as a function of rf power and pressure. Complementary diagnostics and simulations will support benchmarking of sheath-edge localisation and potential profiles.

Acknowledgments

The authors acknowledge the support of the Natural Sciences and Engineering Research Council of Canada (NSERC), Grants No. RGPIN-2019-04333 and No. RGPIN-2025-05757.

References

[AYF08] H. ABE, M. YONEDA, and N. FUJIWARA, Developments of plasma etching technology for fabricating semiconductor devices, *Japanese Journal of Applied Physics* **47** no. 3R (2008), 1435. doi:[10.1143/JJAP.47.1435](https://doi.org/10.1143/JJAP.47.1435).

[All92] J. E. ALLEN, Probe theory - the orbital motion approach, *Physica Scripta* **45** no. 5 (1992), 497. doi:[10.1088/0031-8949/45/5/013](https://doi.org/10.1088/0031-8949/45/5/013).

[ABR57] J. E. ALLEN, R. L. F. BOYD, and P. REYNOLDS, The collection of positive ions by a probe immersed in a plasma, *Proceedings of the Physical Society. Section B* **70** no. 3 (1957), 297–304. doi:[10.1088/0370-1301/70/3/303](https://doi.org/10.1088/0370-1301/70/3/303).

[And00] A. ANDERS, *Handbook of Plasma Immersion Ion Implantation and Deposition*, John Wiley and Sons, Inc, 2000.

[And02] A. ANDERS, From plasma immersion ion implantation to deposition: a historical perspective on principles and trends, *Surface and Coatings Technology* **156** no. 1 (2002), 3–12, Proceedings of the VIth International Conference on Plasma-Based Ion Implantation. doi:[10.1016/S0257-8972\(02\)00066-X](https://doi.org/10.1016/S0257-8972(02)00066-X).

[BCD95] G. BACHET, L. CHÉRIGIER, and F. DOVEIL, Ion velocity distribution function observations in a multipolar argon discharge, *Physics of Plasmas* **2** no. 5 (1995), 1782–1788. doi:[10.1063/1.871328](https://doi.org/10.1063/1.871328).

[BESF26] H. BAHARI, E. EBRAHIMIBASABI, S. M. SADATI, and M. FATHI, Enhancing ion current density in multicusp ion sources: Insights from magnetic field design and experimental validation, *Nuclear Instruments and Methods in Physics Research Section A: Accelerators, Spectrometers, Detectors and Associated Equipment* **1081** (2026), 170920. doi:[10.1016/j.nima.2025.170920](https://doi.org/10.1016/j.nima.2025.170920).

[BPAK15] S. BHATT, J. PULPYTEL, and F. AREFI-KHONSARI, Low and atmospheric plasma polymerisation of nanocoatings for bio-applications, *Surface Innovations* **3** no. 2 (2015), 63–83. doi:[10.1680/sufi.14.00008](https://doi.org/10.1680/sufi.14.00008).

[BS03] R. F. BOIVIN and E. E. SCIME, Laser induced fluorescence in Ar and He plasmas with a tunable diode laser, *Review of Scientific Instruments* **74** no. 10 (2003), 4352–4360. doi:[10.1063/1.1606095](https://doi.org/10.1063/1.1606095).

[BS06] M. P. BRADLEY and C. STEENKAMP, Time-resolved ion and electron current measurements in pulsed plasma sheaths, *IEEE transactions on Plasma Science* **34** no. 4 (2006), 1156–1159. doi:[10.1109/TPS.2006.877744](https://doi.org/10.1109/TPS.2006.877744).

[BMB⁺17] L. BRUCHHAUS, P. MAZAROV, L. BISCHOFF, J. GIERAK, A. D. WIECK, and H. HÖVEL, Comparison of technologies for nano device prototyping with a special focus on ion beams: A review, *Applied Physics Reviews* **4** no. 1 (2017). doi:[10.1063/1.4972262](https://doi.org/10.1063/1.4972262).

[CPT⁺20] C. CATANIO BORTOLAN, C. PATERNOSTER, S. TURGEON, C. PAOLETTI, M. CABIBBO, N. LECIS, and D. MANTOVANI, Plasma-immersion ion implantation surface oxidation on a cobalt-chromium alloy for biomedical applications, *Biointerphases* **15** no. 4 (2020), 041004. doi:[10.1116/6.0000278](https://doi.org/10.1116/6.0000278).

[CB11] P. CHABERT and N. BRAITHWAITE, *Physics of Radio-Frequency Plasmas*, Cambridge University Press, 2011. doi:[10.1017/CBO9780511974342](https://doi.org/10.1017/CBO9780511974342).

[CRWAA91] P. CHATTERTON, J. REES, W. WU, and K. AL-ASSADI, A self-compensating Langmuir probe for use in rf (13.56 mhz) plasma systems, *Vacuum* **42** no. 7 (1991), 489–493. doi:[10.1016/0042-207X\(91\)90022-B](https://doi.org/10.1016/0042-207X(91)90022-B).

[Che03] F. F. CHEN, Langmuir probe diagnostics, in *Mini-Course on Plasma Diagnostics, IEEE ICOPS meeting, Jeju, Korea*, 2003, pp. 20–111.

[CYL95] T. CHUNG, H. YOON, and J. LEE, Scaling laws verification for capacitive rf-discharge Ar plasma using particle-in-cell simulations, *Journal of Applied Physics* **78** no. 11 (1995), 6441–6447. doi:[10.1063/1.360527](https://doi.org/10.1063/1.360527).

[CBSD06] N. CLAIRE, G. BACHET, U. STROTH, and F. DOVEIL, Laser-induced-fluorescence observation of ion velocity distribution functions in a plasma sheath, *Physics of Plasmas* **13** no. 6 (2006), 062103. doi:[10.1063/1.2206786](https://doi.org/10.1063/1.2206786).

[CRD⁺87] J. R. CONRAD, J. L. RADTKE, R. A. DODD, F. J. WORZALA, and N. C. TRAN, Plasma source ion-implantation technique for surface modification of materials, *Journal of Applied Physics* **62** no. 11 (1987), 4591–4596. doi:[10.1063/1.339055](https://doi.org/10.1063/1.339055).

[CM15] D. COULETTE and G. MANFREDI, Collisionless "thermalization" in the sheath of an argon discharge, *Physics of Plasmas* **22** no. 4 (2015), 043505. doi:[10.1063/1.4917239](https://doi.org/10.1063/1.4917239).

[DMRS01] T. DAUBE, P. MEYER, K.-U. RIEMANN, and H. SCHMITZ, Relaxation phenomena in pulsed discharges, *Journal of Applied Physics* **91** no. 4 (2001), 1787–1796. doi:[10.1063/1.1430895](https://doi.org/10.1063/1.1430895).

[DK13] V. M. DONNELLY and A. KORNBLIT, Plasma etching: Yesterday, today, and tomorrow, *Journal of Vacuum Science & Technology A* **31** no. 5 (2013), 050825. doi:[10.1116/1.4819316](https://doi.org/10.1116/1.4819316).

[EH92] G. A. EMMERT and M. A. HENRY, Numerical simulation of plasma sheath expansion, with applications to plasma-source ion implantation, *Journal of Applied Physics* **71** no. 1 (1992), 113–117. doi:[10.1063/1.350740](https://doi.org/10.1063/1.350740).

[GYWC20] L. GEYAO, D. YANG, C. WANGLIN, and W. CHENGYONG, Development and application of physical vapor deposited coatings for medical devices: A review, *Procedia CIRP* **89** (2020), 250–262, 4th CIRP Conference on Biomanufacturing. doi:[10.1016/j.procir.2020.05.149](https://doi.org/10.1016/j.procir.2020.05.149).

[GPA93] V. A. GODYAK, R. B. PIEJAK, and B. M. ALEXANDROVICH, Probe diagnostics of non-Maxwellian plasmas, *Journal of Applied Physics* **73** no. 8 (1993), 3657–3663. doi:[10.1063/1.352924](https://doi.org/10.1063/1.352924).

[GPA02] V. A. GODYAK, R. B. PIEJAK, and B. M. ALEXANDROVICH, Electron energy distribution function measurements and plasma parameters in inductively coupled argon plasma, *Plasma Sources Science and Technology* **11** no. 4 (2002), 525. doi:[10.1088/0963-0252/11/4/320](https://doi.org/10.1088/0963-0252/11/4/320).

[vdG97] M. VAN DE GRIFT, *A diagnostic study on two low pressure plasma sources*, Ph.D. thesis, Technische Universiteit Eindhoven, 1997. doi:[10.6100/IR501160](https://doi.org/10.6100/IR501160).

[GBLH12] J. T. GUDMUNDSSON, N. BRENNING, D. LUNDIN, and U. HELMERSSON, High power impulse magnetron sputtering discharge, *Journal of Vacuum Science and Technology A: Vacuum, Surfaces, and Films* **30** no. 3 (2012), 030801. doi:[10.1116/1.3691832](https://doi.org/10.1116/1.3691832).

[Heb96] G. A. HEBNER, Spatially resolved, excited state densities and neutral and ion temperatures in inductively coupled argon plasmas, *Journal of Applied Physics* **80** no. 5 (1996), 2624– 2636. doi:[10.1063/1.363178](https://doi.org/10.1063/1.363178).

[HGWC93] J. HOPWOOD, C. R. GUARNIERI, S. J. WHITEHAIR, and J. J. CUOMO, Langmuir probe measurements of a radio frequency induction plasma, *Journal of Vacuum Science and Technology A: Vacuum, Surfaces, and Films* **11** no. 1 (1993), 152–156. doi:[10.1116/1.578282](https://doi.org/10.1116/1.578282).

[HBU⁺96] T. HORI, M. D. BOWDEN, K. UCHINO, K. MURAOKA, and M. MAEDA, Measurements of electron temperature, electron density, and neutral density in a radio-frequency inductively coupled plasma, *Journal of Vacuum Science and Technology A: Vacuum, Surfaces, and Films* **14** no. 1 (1996), 144–151. doi:[10.1116/1.579911](https://doi.org/10.1116/1.579911).

[HO83] R. HUTCHINGS and W. C. OLIVER, A study of the improved wear performance of nitrogen-implanted Ti-6Al-4V, *Wear* **92** no. 1 (1983), 143–153. doi:[10.1016/0043-1648\(83\)90014-5](https://doi.org/10.1016/0043-1648(83)90014-5).

[JBT⁺12] M. V. JACOB, K. BAZAKA, D. TAGUCHI, T. MANAKA, and M. IWAMOTO, Electron-blocking hole-transport polyterpenol thin films, *Chemical Physics Letters* **528** (2012), 26–28. doi:[10.1016/j.cplett.2012.01.031](https://doi.org/10.1016/j.cplett.2012.01.031).

[JFGB20] Y. JIANG, G. FUBIANI, L. GARRIGUES, and J. P. BOEUF, Magnetic cusp confinement in low- β plasmas revisited, *Physics of Plasmas* **27** no. 11 (2020), 113506. doi:[10.1063/5.0014058](https://doi.org/10.1063/5.0014058).

[JYG⁺23] C. JIN, C.-S. YIP, Y.-C. GHIM, W. ZHANG, D. JIANG, and G. S. XU, Parametrization of electron sheath expansion for langmuir probe I-V traces, *Journal of Instrumentation* **18** no. 07 (2023), P07009. doi:[10.1088/1748-0221/18/07/P07009](https://doi.org/10.1088/1748-0221/18/07/P07009).

[JLC96] E. C. JONES, B. P. LINDER, and N. W. CHEUNG, Plasma immersion ion implantation for electronic materials, *Japanese Journal of Applied Physics, Part 1: Regular Papers and Short Notes and Review Papers* **35** no. 2S (1996), 1027. doi:[10.1143/JJAP.35.1027](https://doi.org/10.1143/JJAP.35.1027).

[JCM06] S. JUN, H. Y. CHANG, and R. McWILLIAMS, Diode laser-induced fluorescence measurements of metastable argon ions in a magnetized inductively coupled plasma, *Physics of Plasmas* **13** no. 5 (2006), 052512. doi:[10.1063/1.2201894](https://doi.org/10.1063/1.2201894).

[KKK⁺21] P. KARAR, G. KUMAR, R. KAR, H. M. KEWLANI, D. S. PATIL, and R. O. DUSANE, Langmuir probe diagnostics of inductively coupled plasma generated using flat spiral antenna, *IEEE Transactions on Plasma Science* **49** no. 2 (2021), 615–623. doi:[10.1109/TPS.2020.3020977](https://doi.org/10.1109/TPS.2020.3020977).

[KSB04] A. M. KEESEE, E. E. SCIME, and R. F. BOIVIN, Laser-induced fluorescence measurements of three plasma species with a tunable diode laser, *Review of Scientific Instruments* **75** no. 10 (2004), 4091–4093. doi:[10.1063/1.1787166](https://doi.org/10.1063/1.1787166).

[KHG94] E. R. KEITER, W. N. G. HITCHON, and M. J. GOECKNER, A kinetic model of pulsed sheaths, *Physics of Plasmas* **1** no. 11 (1994), 3709–3712. doi:[10.1063/1.870906](https://doi.org/10.1063/1.870906).

[Kho19] A. KHODAEE, *RF-compensated Langmuir Probe Diagnostics of Pulsed Plasma Ion Implantation System*, Master's thesis, University of Saskatchewan, 12 2019.

[KK17] Y. KIM and H. KOWN, Ultra-shallow junction formation on 3D silicon and germanium device structures by ion energy decoupled plasma doping, in *2017 17th International Workshop on Junction Technology (IWJT)*, IEEE, 2017, pp. 62–65. doi:[10.23919/IWJT.2017.7966516](https://doi.org/10.23919/IWJT.2017.7966516).

[KJBR23] C.-P. KLAGES, A. JUNG, M. L. BETZ, and V. RAEV, Low-temperature plasma oxidation of aluminum by Ar-O₂ mixtures in a dielectric-barrier discharge reactor, *Plasma Chemistry and Plasma Processing* **43** no. 5 (2023), 933–955. doi:[10.1007/s11090-023-10352-9](https://doi.org/10.1007/s11090-023-10352-9).

[KKT⁺23] S. T. KOSONEN, T. KALVAS, V. TOIVANEN, O. TARVAINEN, and D. FAIRCLOTH, Critical assessment of the applicability of the Child-Langmuir law to plasma ion source extraction systems, *Plasma Sources Science and Technology* **32** no. 7 (2023), 075005. doi:[10.1088/1361-6595/ace0d7](https://doi.org/10.1088/1361-6595/ace0d7).

[KBA⁺07] P. KOUAKOU, V. BRIEN, B. ASSOUAR, V. HODY, M. BELMAHI, H. N. MIGEON, and J. BOUGDIRA, Preliminary synthesis of carbon nitride thin films by N₂/CH₄ microwave plasma assisted chemical vapour deposition: Characterisation of the discharge and the obtained films, *Plasma Processes and Polymers* **4** no. S1 (2007), S210–S214. doi:[10.1002/ppap.200730703](https://doi.org/10.1002/ppap.200730703).

[KLW21] A. KUMAR, W. H. LEE, and Y. L. WANG, Optimizing the isotropic etching nature and etch profile of Si, Ge and Si0.8Ge0.2 by controlling CF₄ atmosphere with Ar and O₂ additives in ICP, *IEEE Transactions on Semiconductor Manufacturing* **34** no. 2 (2021), 177–184. doi:[10.1109/TSM.2021.3057100](https://doi.org/10.1109/TSM.2021.3057100).

[LKL⁺22] H. LEE, N.-K. KIM, M.-G. LEE, J.-W. KWON, S. H. SON, N. BAE, T. PARK, S. PARK, and G.-H. KIM, Investigation of ion collision effect on electrostatic sheath formation in weakly ionized and weakly collisional plasma, *Plasma Sources Science and Technology* **31** no. 8 (2022), 084006. doi:[10.1088/1361-6595/ac7f52](https://doi.org/10.1088/1361-6595/ac7f52).

[LSK⁺17] H.-C. LEE, B. H. SEO, D.-C. KWON, J. H. KIM, D. J. SEONG, S. J. OH, C.-W. CHUNG, K. H. YOUNG, and C. SHIN, Evolution of electron temperature in inductively coupled plasma, *Applied Physics Letters* **110** no. 1 (2017), 014106. doi:[10.1063/1.4971980](https://doi.org/10.1063/1.4971980).

[LL94] M. A. LIEBERMAN and A. LICHTENBERG, *Principle of Plasma Discharges and Materials Processing*, 3 ed., **1**, John Wiley and Sons, Inc, 1994.

[LM73] R. LIMPAECHER and K. R. MACKENZIE, Magnetic multipole containment of large uniform collisionless quiescent plasmas, *Review of Scientific Instruments* **44** no. 6 (1973), 726–731. doi:[10.1063/1.1686231](https://doi.org/10.1063/1.1686231).

[LZF⁺20] W. Y. L. LING, S. ZHANG, H. FU, M. HUANG, J. QUANSAH, X. LIU, and N. WANG, A brief review of alternative propellants and requirements for pulsed plasma thrusters in micropropulsion applications, *Chinese Journal of Aeronautics* **33** no. 12 (2020), 2999–3010. doi:[10.1016/j.cja.2020.03.024](https://doi.org/10.1016/j.cja.2020.03.024).

[Man92] S. MANTL, Ion beam synthesis of epitaxial silicides: fabrication, characterization and applications, *Materials Science Reports* **8** no. 1 (1992), 1–95. doi:[10.1016/0920-2307\(92\)90006-M](https://doi.org/10.1016/0920-2307(92)90006-M).

[MUOG11] C. B. MELLO, M. UEDA, R. M. OLIVEIRA, and J. A. GARCIA, Corrosion effects of plasma immersion ion implantation-enhanced Cr deposition on SAE 1070 carbon steel, *Surface and Coatings Technology* **205** (2011), S151–S156. doi:[10.1016/j.surfcoat.2011.01.030](https://doi.org/10.1016/j.surfcoat.2011.01.030).

[MI96] J. MENARD and T. INTRATOR, Laboratory measurements and optimization of inductively coupled loop antenna plasma sources, *Plasma Sources Science and Technology* **5** no. 3 (1996), 363–370. doi:[10.1088/0963-0252/5/3/003](https://doi.org/10.1088/0963-0252/5/3/003).

[Mer07] R. L. MERLINO, Understanding Langmuir probe current-voltage characteristics, *American Journal of Physics* **75** no. 12 (2007), 1078–1085. doi:[10.1119/1.2772282](https://doi.org/10.1119/1.2772282).

[MP12] M. MOISAN and J. PELLETIER, *Physics of Collisional Plasmas: Introduction to High-Frequency Discharges*, Springer Science and Business Media, 2012. doi:[10.1007/978-94-007-4558-2](https://doi.org/10.1007/978-94-007-4558-2).

[MKO⁺21] J. MORENO, A. KHODAEE, D. OKERSTROM, M. P. BRADLEY, and L. COUËDEL, Time-resolved evolution of plasma parameters in a plasma immersion ion implantation source, *Physics of Plasmas* **28** no. 12 (2021), 123523. doi:[10.1063/5.0063610](https://doi.org/10.1063/5.0063610).

[Mor23] J. MORENO, *Characterization of an Inductively-Coupled Plasma Immersion Ion Implantation System*, Phd thesis, University of Saskatchewan, September 2023, Available at <https://hdl.handle.net/10388/15061>.

[OAH01] L. OKSUZ, M. ATTA KHEDR, and N. HERSHKOWITZ, Laser induced fluorescence of argon ions in a plasma presheath, *Physics of Plasmas* **8** no. 5 (2001), 1729–1733. doi:[10.1063/1.1358312](https://doi.org/10.1063/1.1358312).

[OH05] L. OKSUZ and N. HERSHKOWITZ, Plasma, presheath, collisional sheath and collisionless sheath potential profiles in weakly ionized, weakly collisional plasma, *Plasma Sources Science and Technology* **14** (2005), 201–208. doi:[10.1088/0963-0252/14/1/022](https://doi.org/10.1088/0963-0252/14/1/022).

[PK02] I.-W. PARK and K. H. KIM, Coating materials of TiN, Ti-Al-N, and Ti-Si-N by plasma-enhanced chemical vapor deposition for mechanical applications, *Journal of Materials Processing Technology* **130-131** (2002), 254–259. doi:[10.1016/S0924-0136\(02\)00807-5](https://doi.org/10.1016/S0924-0136(02)00807-5).

[QCL⁺91] X. Y. QIAN, N. W. CHEUNG, M. A. LIEBERMAN, M. I. CURRENT, P. K. CHU, W. L. HARRINGTON, C. W. MAGEE, and E. M. BOTNICK, Sub-100 nm p+/n junction formation using plasma immersion ion implantation, *Nuclear Instruments and Methods in Physics Research Section B: Beam Interactions with Materials and Atoms* **55** no. 1–4 (1991), 821–825. doi:[10.1016/0168-583X\(91\)96286-T](https://doi.org/10.1016/0168-583X(91)96286-T).

[Rie91] K.-U. RIEMANN, The bohm criterion and sheath formation, *Journal of Physics D: Applied Physics* **24** no. 4 (1991), 493. doi:[10.1088/0022-3727/24/4/001](https://doi.org/10.1088/0022-3727/24/4/001).

[SVV⁺97] N. SADEGHI, M. VAN DE GRIFT, D. VENDER, G. M. KROESEN, and F. J. DE HOOG, Transport of argon ions in an inductively coupled high-density plasma reactor, *Applied Physics Letters* **70** no. 7 (1997), 835–837. doi:[10.1063/1.118218](https://doi.org/10.1063/1.118218).

[SNTG91] N. SADEGHI, T. NAKANO, D. J. TREVOR, and R. A. GOTTSCHO, Ion transport in an electron cyclotron resonance plasma, *Journal of Applied Physics* **70** no. 5 (1991), 2552–2569. doi:[10.1063/1.350332](https://doi.org/10.1063/1.350332).

[SR05] H. SALAMI and A. J. ROSS, A molecular iodine atlas in ascii format, *Journal of Molecular Spectroscopy* **233** no. 1 (2005), 157–159. doi:[10.1016/j.jms.2005.06.002](https://doi.org/10.1016/j.jms.2005.06.002).

[SB07] C. J. T. STEENKAMP and M. P. BRADLEY, Active charge/discharge IGBT modulator for Marx generator and plasma applications, *IEEE Transactions on Plasma Science* **35** no. 2 (2007), 473–478. doi:[10.1109/TPS.2007.892739](https://doi.org/10.1109/TPS.2007.892739).

[SL91] R. A. STEWART and M. A. LIEBERMAN, Model of plasma immersion ion implantation for voltage pulses with finite rise and fall times, *Journal of Applied Physics* **70** no. 7 (1991), 3481–3487. doi:[10.1063/1.349240](https://doi.org/10.1063/1.349240).

[SERO04] Y. SUKHANOV, A. ERSHOV, K. RUDENKO, and A. ORLIKOVSKY, Comparative study of inductively coupled and microwave BF₃ plasmas for microelectronic technology applications, *Proceedings of SPIE - The International Society for Optical Engineering* **5401** (2004). doi:[10.1117/12.556998](https://doi.org/10.1117/12.556998).

[TCBH07] K. TAKASHI, C. CHARLES, R. BOSWELL, and R. HATAKEYAMA, *Pulsed Electrostatic Langmuir Probe Technique for Electron Energy Distribution Function Measurement in Radio-Frequency-Driven Plasmas*, Tech. Report 2, The Australian National University, 2007.

[TUD07] H. TELLE, A. URENA, and R. DONOVAN, *Laser Chemistry: spectroscopy, dynamics and applications*, 1, John Wiley and Sons, Ltd., 2007.

[TC00] X. TIAN and P. CHU, Modeling of the relationship between implantation parameters and implantation dose during plasma immersion ion implantation, *Physics Letters, Section A: General, Atomic and Solid State Physics* **277** no. 1 (2000), 42–46. doi:[10.1016/S0375-9601\(00\)00673-3](https://doi.org/10.1016/S0375-9601(00)00673-3).

[UBC05] M. UEDA, L. A. BERNI, and R. M. CASTRO, Application of Plasma Immersion Ion Implantation for improved performance of tools and industrial components, *Surface and Coatings Technology* **200** no. 1-4 SPEC. ISS. (2005), 517–520. doi:[10.1016/j.surfcoat.2005.02.146](https://doi.org/10.1016/j.surfcoat.2005.02.146).

[VPL⁺05] D. VEMPAIRE, J. PELLETIER, A. LACOSTE, S. BÉCHU, J. SIROU, S. MIRAGLIA, and D. FRUCHART, Plasma-based ion implantation: A valuable technology for the elaboration of innovative materials and nanostructured thin films, *Plasma Physics and Controlled Fusion* **47** no. 5 A (2005), A153. doi:[10.1088/0741-3335/47/5A/011](https://doi.org/10.1088/0741-3335/47/5A/011).

[VCHd06] P. VERDONCK, P. B. CALÍOPE, E. D. M. HERNANDEZ, and A. N. R. DA SILVA, Plasma etching of electrospun polymeric nanofibres, *Thin Solid Films* **515** no. 2 (2006), 831–834, Proceedings of the Eighth International Conference on Atomically Controlled Surfaces, Interfaces and Nanostructures and the Thirteenth International Congress on Thin Films. doi:[10.1016/j.tsf.2005.12.196](https://doi.org/10.1016/j.tsf.2005.12.196).

[WMD93] D. WANG, T. MA, and X. DENG, Model of collisional sheath evolution in plasma source ion implantation, *Journal of Applied Physics* **74** no. 4 (1993), 2986–2988. doi:[10.1063/1.354612](https://doi.org/10.1063/1.354612).

[WHCW08] K.-W. WENG, S. HAN, Y.-C. CHEN, and D.-Y. WANG, Characteristics of diamond-like carbon film deposited by filter arc deposition, *Journal of Materials Processing Technology* **203** no. 1-3 (2008), 117–120. doi:[10.1016/j.jmatprotec.2007.09.061](https://doi.org/10.1016/j.jmatprotec.2007.09.061).

[Woo93] B. WOOD, Displacement current and multiple pulse effects in plasma source ion implantation, *Journal of Applied Physics* **73** no. 10 (1993), 4770–4778. doi:[10.1063/1.353841](https://doi.org/10.1063/1.353841).

[YTY93] K. YAMAUCHI, K. TAKAHASHI, and E. YABE, rf plasma source using a magnetic line-cusp field, *Review of Scientific Instruments* **64** no. 9 (1993), 2434–2439. doi:[10.1063/1.1143901](https://doi.org/10.1063/1.1143901).

[YHS15] C. YIP, N. HERSHKOWITZ, and G. SEVERN, Verifying effects of instability enhanced ion-ion Coulomb collisions on ion velocity distribution functions near the sheath edge in low temperature plasmas, *Plasma Sources Science and Technology* **24** no. 1 (2015), 015018. doi:[10.1088/0963-0252/24/1/015018](https://doi.org/10.1088/0963-0252/24/1/015018).

[YB23] T. YOUSAF and M. P. BRADLEY, Helium plasma immersion ion implantation studies of tungsten and tungsten heavy alloys for fusion plasma facing components, *Radiation Effects and Defects in Solids* **178** no. 1–2 (2023), 143–159. doi:[10.1080/10420150.2023.2186877](https://doi.org/10.1080/10420150.2023.2186877).

[YC94] C. YU and N. W. CHENNG, Trench doping conformality by plasma immersion ion implantation (PIII), *IEEE Electron Device Letters* **15** no. 6 (1994), 196–198. doi:[10.1109/55.286690](https://doi.org/10.1109/55.286690).

[ZZZ13] Y. ZHANG, L. ZHANG, and C. ZHOU, Review of chemical vapor deposition of graphene and related applications, *Accounts of Chemical Research* **46** no. 10 (2013), 2329–2339. doi:[10.1021/ar300203n](https://doi.org/10.1021/ar300203n).